Interface engineering of ferroelectricity in thin films of thiophosphate ABP_2X_6 (A = Cu, Ag; B = In, Bi, Cr, V; X = S, Se)

Guoliang Yu,[1] Anlian Pan,[2] and Mingxing Chen [1,*]

[1]*Key Laboratory for Matter Microstructure and Function of Hunan Province, Key Laboratory of Low-Dimensional Quantum Structures and Quantum Control of Ministry of Education, School of Physics and Electronics, Hunan Normal University, Changsha 410081, China*
[2]*Key Laboratory for Micro-Nano Physics and Technology of Hunan Province, College of Materials Science and Engineering, Hunan University, Changsha 410082, China*

Two-dimensional ferroelectrics (FEs) are promising in the miniaturization of memory devices with ultrahigh-density data storage and low power consumption. However, many thiophosphate monolayers, i.e., analogs of $CuInP_2S_6$ and referred to as ABP_2X_6, lose ferroelectricity and instead exhibit an antiferroelectric (AFE) or paraelectric ordering. We propose to tune the AFE ABP_2X_6 monolayers into the FE ordering through interface engineering. The mechanism is that there are couplings between the charge polarizations of the ABP_2X_6 monolayers and the local dipoles as well as the induced electronic polarizations in the substrate which have a tendency to stabilize the FE ordering. We further perform first-principles calculations for $CuInP_2Se_6$ and $CuCrP_2S_6$ monolayers and their van der Waals heterostructures. We find that an AFE $CuInP_2Se_6$ monolayer becomes FE as interfaced with graphene, MoS_2, and h-BN monolayers. In contrast, the $CuCrP_2S_6$ monolayer remains AFE since there is a large energy difference between the AFE and FE phases. Interfacing it with a $MoTe_2$ monolayer induces a metal-insulator transition for the heterostructure, whereas interfacing with a polar surface MgO(111) can drive it into FE. The interfacing effect can also be used to manipulate the FE properties of ABP_2X_6 multilayers. We further find that the AFE-to-FE transition is electrically switchable in these systems. In particular, it is accompanied by an indirect-direct band-gap transition for the $CuInP_2Se_6$ monolayer. Our study offers an effective approach to tune the FE and electronic properties of ABP_2X_6 thin films for applications in electronics and optoelectronics.

I. INTRODUCTION

Ferroelectric (FE) memory devices that allow nonvolatile and fast read-write processes are promising in ultra-high-density data storage with low power consumption. Conventional FEs, such as perovskite oxides, lose ferroelectricity as their thickness is reduced to a few nanometers due to the depolarization field [1–5]. Therefore, preserving ferroelectricity in the monolayer limit has long been an important issue in the field of FEs, which is desired for miniaturization of the devices. Recent studies found that group-IV monochalcogenide monolayers exhibit ferroelectricity with high Curie temperatures [6–8]. In these systems, charge polarizations are in-plane, which are merely affected by the depolarization field perpendicular to the systems. Notably, recent studies found that α-In_2Se_3 monolayer and $CuInP_2S_6$ thin films possess out-of-plane polarizations [9–13].

The above discoveries have inspired a great number of explorations of ferroelectricity in layered two-dimensional (2D) materials [14–23]. In particular, a number of analogs of copper indium thiophosphate $CuInP_2S_6$ monolayer, which are referred to as ABP_2X_6, were predicted to exhibit ferroelectricity and ferromagnetism simultaneously [24,25]. However,

like the conventional perovskite FEs, ferroelectricity in these materials is vanishing as the materials approaching the monolayer limit. Instead, the antiferroelectric (AFE) phase has a lower energy than that of the FE phase as revealed by density-functional theory (DFT) calculations [22,24–29]. Moreover, experiment finds coexistence of FE and AFE states in $CuInP_2Se_6$ [30]. In fact, many ABP_2X_6 members suffer from the problem that the FE ordering is no longer the ground state (see Table I); that is, the paraelectric (PE) or AFE ordering becomes energetically more favorable than the FE ordering. This fact is unfavorable for their applications in FE devices and miniaturization of the devices. Thus, it is of importance to manipulate the ferroelectricity in these systems for practical device applications.

In this paper, we find that interface can be used to tune the FE properties of ABP_2X_6 monolayers and multilayers. We provide an energy augment that involves a coupling between the charge polarizations of the monolayers and dipoles of the substrates. This coupling lowers the energy of one FE ordering while keeping that of the AFE ordering unchanged and thus may change their relative stabilities. We illustrate the idea in $CuInP_2Se_6$ and $CuCrP_2S_6$ monolayers by performing first-principles calculations. Moreover, we find that the $CuInP_2Se_6$ monolayer undergoes an indirect-to-direct band-gap transition as it transforms from the AFE ordering to the FE ones, which can be tuned ferroelectrically and holds potential applications in electronics and optoelectronics.

*mxchen@hunnu.edu.cn

224102-1

TABLE I. Energies of ABP_2X_6 monolayers. U_0 (U_1) denotes the energy difference between the PE and FE (AFE) phases, i.e., $U_0 = E_{PE} - E_{FE}$ ($U_1 = E_{PE} - E_{AFE}$). $\Delta E = E_{FE} - E_{AFE}$. E_i represent the total energies of ABP_2X_6. Data of U_0, U_1, and ΔE are not available for $AgInP_2S_6$ and $AgInP_2Se_6$ monolayers due to that the structures for the AFE and FE phases were relaxed to the PE phase during our DFT calculations. GS denotes the ground state. The systems are classified into two categories by U_0 vs ΔE.

Systems	U_0 (meV)	U_1 (meV)	ΔE (meV)	GS	Type
$CuInP_2S_6$	218	242	24	AFE	I
$CuInP_2Se_6$	83	95	12	AFE	I
$CuBiP_2S_6$	269	272	3	AFE	I
$CuBiP_2Se_6$	121	104	-17	FE	*
$CuCrP_2S_6$	74	142	68	AFE	I
$CuCrP_2Se_6$	20	69	49	AFE	II
$CuVP_2S_6$	67	139	72	AFE	II
$CuVP_2Se_6$	-7	71	78	AFE	II
$AgInP_2S_6$	N/A	N/A	N/A	PE	*
$AgInP_2Se_6$	N/A	N/A	N/A	PE	*
$AgBiP_2S_6$	44	3	-41	FE	*
$AgBiP_2Se_6$	25	1	-24	FE	*

II. COMPUTATIONAL DETAILS

We use a slab structure to model the monolayers and heterostructures. For $CuInP_2Se_6$-based heterostructures, the slab consists of a 1×1 unit cell of a $CuInP_2Se_6$ monolayer and a 2×2 supercell of a MoS_2 monolayer, whereas for $CuCrP_2S_6$, the slab contains a 1×1 unit cell of a $CuCrP_2S_6$ monolayer and a $\sqrt{3} \times \sqrt{3}$ supercell of a $MoTe_2$ monolayer. These supercells give rise to small lattice mismatches between the overlayers and the substrates ($<2\%$). In addition, for $CuCrP_2S_6$, a polar surface, i.e., MgO(111), is also used as the substrate. For each heterostructure, we investigate the stacking effect by performing calculations for a number of configurations in which the ABP_2X_6 monolayer is artificially shifted with respect to the substrate.

We perform DFT calculations for our systems using the Vienna Ab initio Simulation Package [31]. The pseudopotentials were constructed by the projector augmented wave method [32,33]. Van der Waals (vdW) dispersion forces between the adsorbate and the substrate were accounted for through the DFT-D2 method [34]. Calculations using the DFT-D3 and optPBE-vdW methods were performed for comparison [35,36]. A 15×15 Monkhorst-Pack k-mesh was used to sample the 2D Brillouin zone (BZ) and a plane-wave energy cutoff of 400 eV was used for structural relaxation and electronic structure calculations. Layer projections of band structures were performed by using program KPROJ, which is based on the k-projections method [37–39].

III. RESULTS AND DISCUSSIONS

A. General concept

We begin by investigating the energetics of ABP_2X_6 monolayers obtained from first-principles calculations. We have considered PE, FE, and AFE orderings for all the systems, which are shown in Fig. 1. In the FE and AFE phases, the
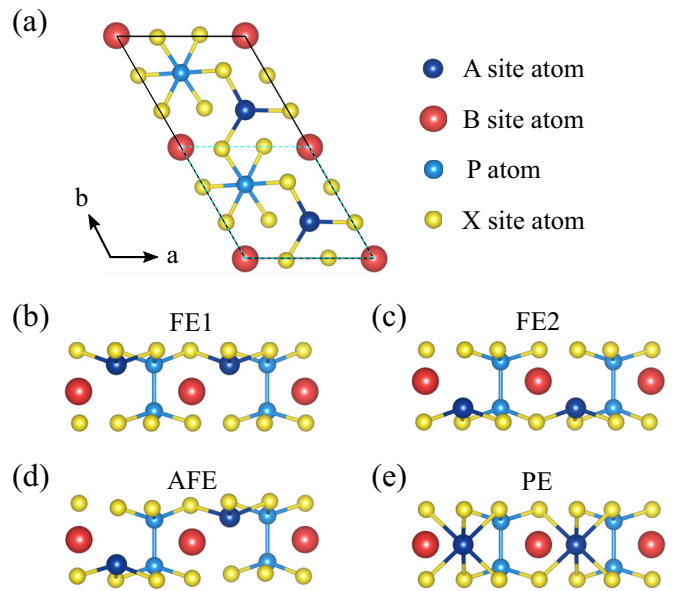

FIG. 1. Geometric properties of a ABP_2X_6 monolayer. (a) Top view of the structure. The green box shows the unit cell of the FE and PE orderings. The black box indicates the cell of the AFE phase, which is a 1×2 supercell of the chemical unit cell. (b), (c) Side views of the FE phases with opposite charge polarizations, which are denoted as FE1 and FE2, respectively. For a free-standing ABP_2X_6 monolayer, they are energetically degenerate. (d), (e) Side views of the AFE and PE phases.

charge polarizations are out of plane mainly due to displacements of A atoms. We use a 1×2 supercell to model the AFE phase in which neighboring unit cells have opposite polarizations. The results are summarized in Table I. One can see that for a number of ABP_2X_6 monolayers (A = Cu; B = In, Cr, V; and X = S, Se), the AFE phase has a lower energy than the PE and FE phases. For the FE phase, there are two energetically degenerate states, which are denoted as FE1 and FE2, respectively. In the presence of a substrate, the degeneracy is expected to be lifted. The trend of our results is in good agreement with previous studies [22,24–29].

We now turn to our idea of interface engineering of ferroelectricity in ABP_2X_6 monolayers, which is shown in Fig. 2. The idea is pretty much similar to FE materials under external electric fields that the polarizations tend to be parallel to the fields. Instead, we make use of dipoles from substrates. The difference between using the electric fields and substrates is that the latter allows a nonvolatile tuning of the phase stability. Figure 2(a) schematically shows the potential energy of a free-standing ABP_2X_6 monolayer as a function of displacement of A atoms. The FE and AFE phases are expected to have double-well-like potentials. For free-standing monolayers, the two FE phases are energetically degenerate. We focus on the systems for which the AFE phase is the ground state. Therefore, the AFE phase is assumed to have a lower energy than the FE phases. We denote the energy difference between the PE and FE phases as $U_0 = E_{PE} - E_{FE}$. Generally, U_0 is the energy barrier for the transform between the two FE phases. Likewise, ΔE denotes the energy difference between the FE and the AFE phases, i.e., $\Delta E = E_{FE} - E_{AFE}$. The potential
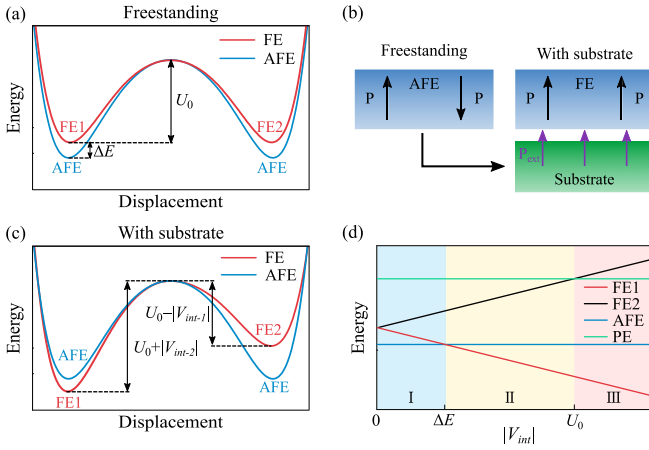
FIG. 2. Interface engineering of ferroelectricity in a monolayer with out-of-plane polarization. (a) Schematic illustration of double-well potentials of a free-standing monolayer for the FE and AFE phases. We assume that the AFE phase has a lower energy than the FE one. U_0 (ΔE) denotes the energy difference between the FE and PE (AFE) phases. (b) Interface induced AFE-to-FE phase transition in a 2D monolayer with out-of-plane polarization. P denotes the charge polarization with arrows showing the direction. P_{ext} represents dipoles of the substrate. (c) Potential energetics of the ABP_2X_6 monolayers with a coupling between P and P_{ext}. The coupling strengths V_{int} for the two FE states and the substrate are expected to be slightly different. (d) Total energies of different phases as a function of V_{int}, i.e., the coupling between P and P_{ext}, and the phase diagram for $\Delta E < U_0$.

energy per unit cell can be expanded into even terms of P based on the Landau-Ginzburg formula. In the presence of external dipoles P_{ext}, there is an additional term that accounts for the coupling of P and P_{ext}. This term, essentially a dipole-dipole interaction, has a form of $-\alpha P \cdot P_{ext}/r^3$, where α is a constant and r is the distance between P and P_{ext}. We denote this term as V_{int}. Then, the potential energy can be written as:

$$E = AP^2 + BP^4 + CP^6 + V_{int}. \tag{1}$$

Therefore, the coupling lifts the degeneracy of the two FE phases: It lowers the total energy of one FE phase while it increases the total energy of the other one. The FE phase with P parallel to P_{ext} is expected to have a lower energy than the one with P antiparallel to P_{ext}. In contrast, the effects of this coupling on the total energies of the AFE and PE phases are expected to be negligible. As a result, the coupling changes the energy differences between the FE and the AFE phases and may thus enhance the stability of the FE phases [Figs. 2(b) and 2(c)]. In ABP_2X_6-based interfaces, two types of dipoles contribute to P_{ext}. One is ion-dipole (P_i) of the substrate such as the Mo-S dipoles in MoS_2. The other one is the induced electronic polarization (P_e) in the substrate owing to the inter-face interaction.

We classify the AFE ABP_2X_6 monolayers listed in Table I into two categories according to comparisons of U_0 and ΔE: $\Delta E < U_0$ for type-I monolayers and $\Delta E \geqslant U_0$ for type-II systems, respectively. For type-I systems, the phase diagram of an AFE monolayer as a function of V_{int} is shown in Fig. 2(d). In region I, the AFE phase remains to be the ground state

since the strength of V_{int} is smaller than ΔE. In region II, the coupling overcomes ΔE but remains smaller than U_0, i.e., $\Delta E < |V_{int}| < U_0$. In this case, FE1 has a lower energy than the AFE phase and FE2 remains to be a local minimum of the potential energy [see Fig. 2(c)]. Therefore, the two FE phases may be switched electrically. In region III, i.e., $|V_{int}| \geqslant U_0$, FE1 remains to be the ground state, whereas FE2 is energetically higher than the PE phase. The coupling strengths V_{int} for the two FE states are expected to be slightly different (the distance between P and P_{ext} is slightly different). Therefore, in Fig. 2(c), we use V_{int-1} and V_{int-2} to denote the two couplings, respectively.

For type-II systems, the FE phases remain energetically higher than the AFE phase when $|V_{int}| < \Delta E$ enhancing the coupling strength such that $|V_{int}| \geqslant \Delta E$ can tune FE1 into the ground state. However, FE2 becomes energetically higher than the PE phase since $\Delta E \geqslant U_0$ (see Appendix B).

B. CuInP₂Se₆-based heterostructures

We now apply the above scheme to specific materials, which are $CuInP_2Se_6$ and $CuCrP_2S_6$ monolayers, respectively. Based on the values of U_0 and ΔE shown in Table. I, both are type-I AFE systems. However, there is a significant difference between them. For the $CuInP_2Se_6$ monolayer, ΔE is small (less than 20 meV) and is much smaller than U_0, whereas for the $CuCrP_2S_6$ monolayer, ΔE is relatively large and is comparable to U_0. We choose different transition-metal dichalcogenide (TMD) monolayers, graphene, and h-BN monolayer as the substrates for the convenience of computation. Although a free-standing TMD monolayer is nonpolar, the local dipoles pointing from the top and bottom chalcogen atoms to the transition metal atoms are expected to have different effects on the total energy of the ABP_2X_6 monolayer. This is because these two types of dipoles have different distances to the dipole of the overlayer. The local dipoles next to the interface will dominate the coupling between the TMD and ABP_2X_6 monolayers.

Figure 3(a) shows the potential energies of a free-standing $CuInP_2Se_6$ monolayer. The energy difference between the PE and the FE phases, i.e., U_0, is about 83 meV. This value is much larger than the energy difference between the FE and the AFE phases, i.e., ΔE (~12 meV). Such a small value of ΔE may be overcome by a vdW-type interfacial interaction between the overlayer and the substrate. We perform calculations of $CuInP_2Se_6/MoS_2$ for a number of configurations. For each configuration, PE, FE1, FE2, and AFE phases are considered. We find that the two layers interact via a vdW-type bonding since there is a large layer distance between them (~3.4 Å). FE2 has the lowest energy for each configuration. Figure 3(b) shows the side view of the lowest energy structure. The structures of other configurations are shown in Appendix C. From Fig. 3(c), one can see that the FE2 phase is about 12 meV lower than the AFE phase. Compared to the free-standing system, this result indicates that a vdW interface can lead to a change of about 24 meV in the total energy of a $CuInP_2Se_6$ monolayer. On the other hand, the FE1 phase is about 25 meV higher than the AFE phase but remains about 77 meV lower than the PE phase. We further investigate the kinetic pathway of FE phase transform for this structure using
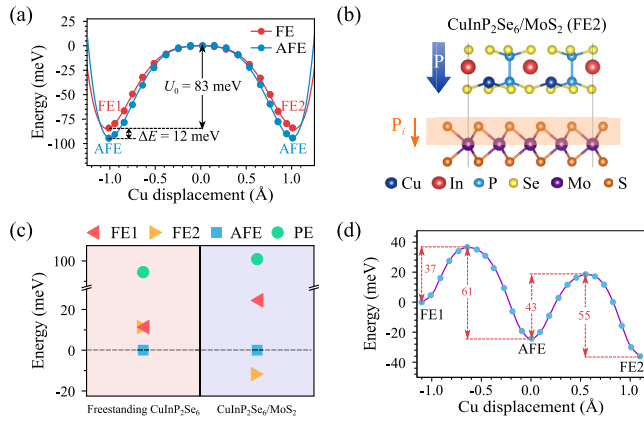
FIG. 3. vdW interface engineering of ferroelectricity in $CuInP_2Se_6$. (a) Potential energies of the FE and AFE phases of a free-standing $CuInP_2Se_6$ monolayer. The values of U_0 and ΔE are shown. (b) Structure of the FE2 phase for $CuInP_2Se_6/MoS_2$. P shows the charge polarization of the $CuInP_2Se_6$ monolayer. P_i denotes the dipoles pointing from the interface S to the Mo atoms (the orange region). (c) Effects of interfacing on energies of a $CuInP_2Se_6$ monolayer. (d) Kinetic pathway of the FE phase transform in $CuInP_2Se_6/MoS_2$. Energy barriers are shown in meV.

FIG. 4. Ferroelectric properties of $CuInP_2Se_6$/graphene and $CuInP_2Se_6$/h-BN. (a) Geometric structure of $CuInP_2Se_6$/graphene and $CuInP_2Se_6$/h-BN in FE2 phase. P_e denotes the electronic polarization from interface interaction. (b) The total energies of a $CuInP_2Se_6$ monolayer with the substrates. (c), (d) The planar-averaged charge-density difference $[\Delta\rho(z)]$ for the two FE orderings, which are obtained by subtracting the density of the PE phase from those of the FE orderings. The red and blue spheres show the centers of the positive and negative densities, respectively. The results for $CuInP_2Se_6$/h-BN are similar to $CuInP_2Se_6$/graphene, which is shown in Appendix D.

the climbing image nudged elastic band (CI-NEB) method [40] for which the results are shown in Fig. 3(d). One can see that the FE2 phase remains to be a local minimum of the energy surface of $CuInP_2Se_6/MoS_2$. Moreover, the barriers between different phases suggest that a nonvolatile switching of the FE phases is feasible.

In addition to the MoS_2 monolayer, we also investigate the effects of interfacing the $CuInP_2Se_6$ monolayer to graphene as well as a h-BN monolayer [Fig. 4(a)]. These substrates are distinct from the TMD monolayers in that they have no out-of-plane local dipoles next to the interface. Figure 4(b) shows that the energy of the FE2 ordering is about 20 (30) meV lower than the AFE phase when as the system is interfaced to graphene (a h-BN monolayer), whereas that of the FE1 phase is increased about 30 meV higher the AFE phase. The enhancements induced by these substrates are even slightly larger than that caused by a MoS_2 monolayer. We further perform analyses over the charge-density difference between the FE and the PE orderings, i.e., $\Delta\rho = \rho_{FE} - \rho_{PE}$, from which the induced electronic polarization P_e in the substrates can be obtained; ρ_{FE} and ρ_{PE} denote the charge densities of the FE and PE orderings. One can see from Figs. 4(c) and 4(d) that P_e is antiparallel and parallel with the polarization P of the FE1 and FE2 orderings of the $CuInP_2Se_6$ monolayer, respectively. Therefore, the coupling between P_e and P lowers (increases) the energy of the FE2 (FE1) phase. We also perform similar analyses for $CuInP_2Se_6/MoS_2$ and find that the electronic polarizations in the MoS_2 monolayer induced by the $CuInP_2Se_6$ are negligibly small (see Appendix D). These results suggest that both the local dipoles of the substrates and the induced electronic polarizations in them are responsible for the enhancement of the FE ordering.

Song *et al.* reveal via first-principles calculations that $CuInP_2Se_6$ thin films with a size of less than six layers show

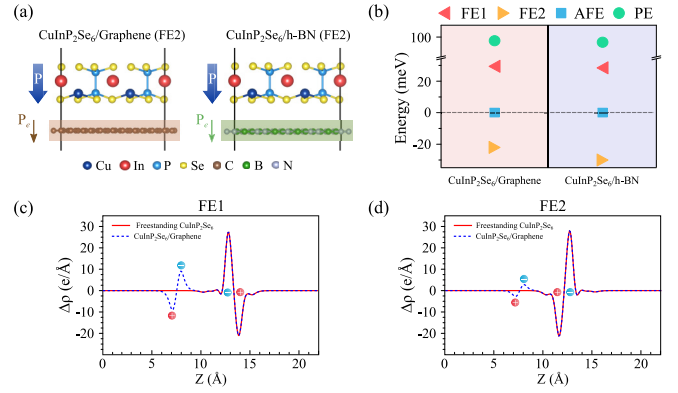AFE ordering within each layer (the layers are ferroelectrically coupled) [26]. Films thicker than the critical size are found to be in the FE ordering. We perform calculations for its bilayer and trilayer supported by a MoS_2 monolayer, for which the results are shown in Fig. 5. One can see that both are turned into FE in the heterostructures. One can expect that thicker multilayers can also be driven into the FE ordering as interfaced with MoS_2, graphene, and h-BN monolayers.
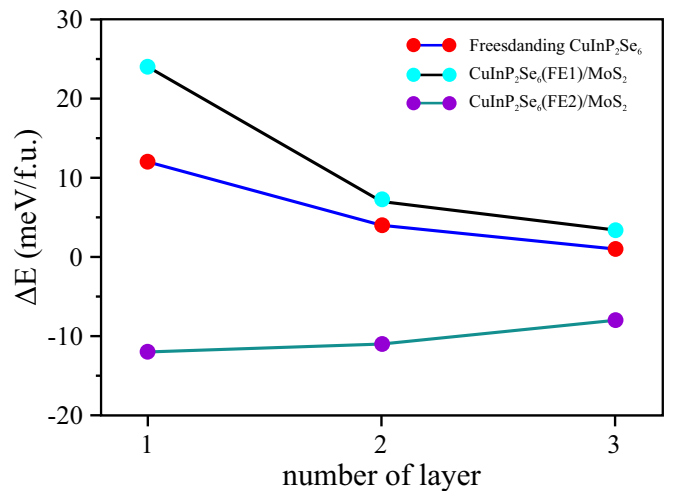

FIG. 5. Interfacing effects on the stabilities of various phases of $CuInP_2Se_6$ multilayers. $\Delta E = E_{FE} - E_{AFE}$, where E_{FE} and E_{AFE} are the total energies of the FE and AFE orderings.
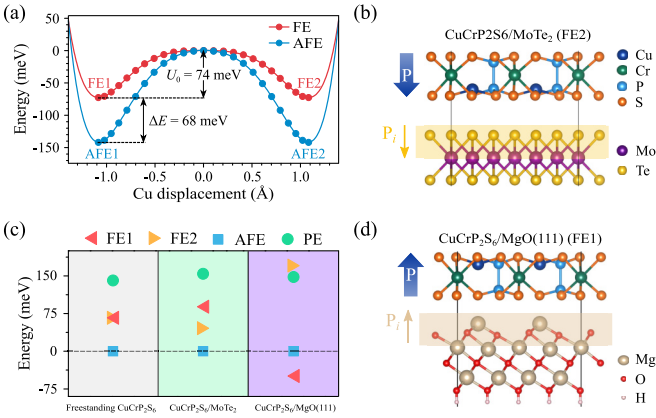
FIG. 6. Interface engineering of ferroelectricity in a $CuCrP_2S_6$ monolayer. (a) Potential energies a free-standing $CuCrP_2S_6$ monolayer. (b) Geometric structure of $CuCrP_2S_6/MoTe_2$ in the FE2 phase. (c) Effects of different substrates on the total energy of a $CuCrP_2S_6$ monolayer. (d) Geometric structure of $CuCrP_2S_6/MgO(111)$ in the FE1 ordering, respectively. In (b) and (d), charge polarizations of the ABP_2X_6 monolayer align parallel to the local dipoles of the substrates next to the overlayer.

C. $CuCrP_2S_6$-based heterostructures

We now discuss the effects of interfacing on the phase stability of a $CuCrP_2S_6$ monolayer. The DFT+U method [41] is used to treat electron correlations due to the partially filled d orbital of Cr for which a value of 3 eV is used [24]. From Fig. 6(a) as well as Table I, one can see that for the free-standing $CuCrP_2S_6$ monolayer, the energy difference between the FE and the AFE phases, i.e., ΔE, is about 68 meV. This value is much larger than the energy change ($\sim$25 meV) for a $CuInP_2Se_6$ monolayer induced by a MoS_2 monolayer substrate. Geometric structures of the $CuCrP_2S_6/MoTe_2$ heterostructures are shown in Figs. 6(b) and Appendix C. The layer distance between the two monolayers is about 3.3 Å, which implies that there is also a vdW-type interaction between them. Indeed, this interaction lowers the total energy of FE2 by about 20 meV. Specifically, the energy difference between it and the AFE phase decreases from 68 meV for the free-standing $CuCrP_2S_6$ monolayer to 46 meV for the supported one. However, the AFE phase remains to be the ground state [see the middle panel of Fig. 6(c)]. Therefore, vdW-type interfaces may not be effective in tuning FE properties of the $CuCrP_2S_6$ monolayer, although they do have a tendency to enhance the stability of the FE2 phase.

We further look at the effects of a polar substrate on the phase stability of the $CuCrP_2S_6$ monolayer. We choose MgO(111) as the substrate since it is a well-known polar surface. Previous studies revealed that this surface demonstrates various surface reconstructions, among which octopolar and p(1 × 2) reconstructions were already experimentally observed [42,43]. In our calculations, the p(1 × 2)-MgO(111) with Mg-termination is used as the substrate for the convenience of computation. The structures for the heterostructures are shown in Figs. 6(d) and Appendix C. Our calculations find that FE1 has a lower energy than the AFE phase by

50 meV. However, the total energy of FE2 is increased about 26 meV higher than the PE phase. Nonetheless, our NEB calculations shown in Appendix E suggest that there may still be a nonvolatile switching between the FE phases.

In addition, we perform calculations for the above $CuInP_2Se_6$- and $CuCrP_2S_6$-based interfaces using different vdW functionals/methods; the results are shown in Appendix F. One can see that these methods give the same trend in the stability of different orderings.

D. Polarization of interfaces

We now discuss the interfacing effects on the polarization of ABP_2X_6 monolayers. We calculate the polarization for each structure by artificially displacing the Cu atoms along the kinetic path FE1-AFE-FE2; the results are shown in Fig. 7. The results for the free-standing $CuInP_2Se_6$ and $CuCrP_2S_6$ monolayers are shown for comparison. For the FE1 state of $CuInP_2Se_6/MoS_2$, the polarization is slightly smaller than that of the free-standing $CuInP_2Se_6$. By contrast, the polarization of the FE2 state is slightly enhanced as a result of interfacing. This behavior is because the induced electronic polarization P_e is opposite to the polarization P of the $CuInP_2Se_6$ monolayer for the FE1 state while parallel with P for the FE2 state.

$CuCrP_2S_6$ shows different trends from $CuInP_2Se_6$ in that the polarizations for both FE states are reduced when it is interfaced with $MoTe_2$ and MgO(111). For the FE1 state of $CuCrP_2S_6/MoTe_2$, the reduction in the total polarization is because the whole system becomes metallic, which can be expected from the band alignments (see Appendix G). Thus, the screening effect reduces the polarization of the interface. For the FE2 state, the polarization reduction is due to that the dipoles of the constituents are antiparallel with each other. For $CuCrP_2S_6/MgO(111)$, the system is metallic in both the FE1 and FE2 phases due to strong interface bondings (see Appendix H). Therefore, a reduction in the total polarization can be naturally expected.

E. Band structure

As already mentioned above for $CuCrP_2S_6/MoTe_2$, the system experiences a metal-insulator transition on a FE switch (see Appendix H). The interfacing effect can also lead to tunable band structure for the $CuInP_2Se_6$ monolayers. Figure 8 shows that the FE phases of a $CuInP_2Se_6$ monolayer have a direct band gap of about 0.99 eV with both the valence band maximum (VBM) and conduction band minimum (CBM) located at Γ. This band-gap size is comparable to that for Si, which is desired for optical applications. In contrast, the AFE phase is an indirect band-gap semiconductor with a gap size of about 1.03 eV. The CBM is located at Γ, whereas the VBM is located at a k point in between the Γ and X point. In the presence of a MoS_2 monolayer, their bands remain almost unchanged. In particular, the nature of an indirect/direct band gap is preserved, which is due to the vdW-type interaction between them. We further confirm that the nature of the band gap is maintained on small strains. We recall that for $CuInP_2Se_6/MoS_2$ heterostructures, the FE2 phase becomes the ground state and the

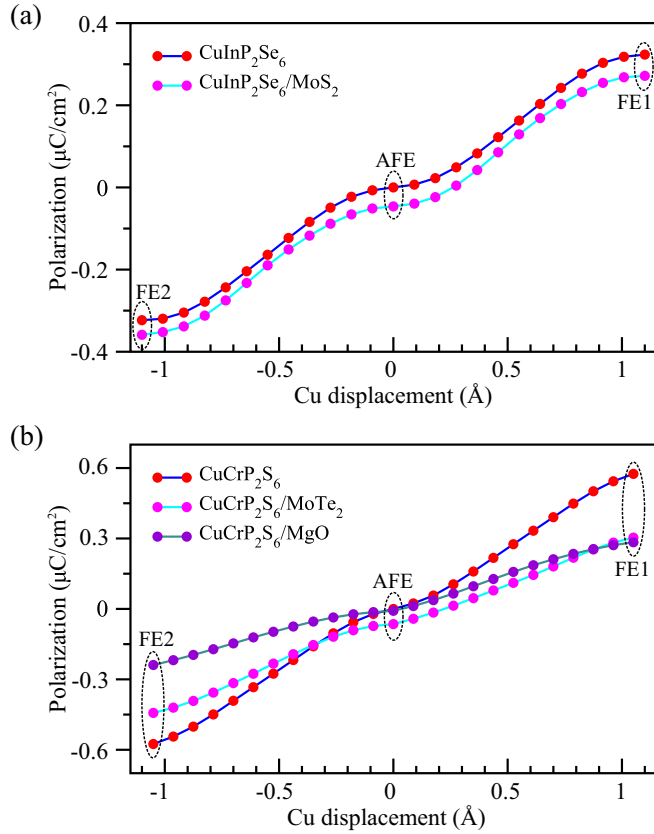FIG. 7. Interfacing effects on the total polarization of $CuInP_2Se_6$ (a) and $CuCrP_2S_6$ (b).

FIG. 8. Effects of a MoS_2 monolayer substrate on the band structure of a $CuInP_2Se_6$ monolayer. (a) and (c) Band structures for a free-standing $CuInP_2Se_6$ monolayer in FE and AFE orderings, respectively. (b) and (d) Corresponding plots for $CuInP_2Se_6/MoS_2$. In (b) and (d), electronic bands are weighted by layer projections onto the $CuInP_2Se_6$ monolayer. The insets show the BZs of the $CuInP_2Se_6$ monolayer in different phases.

FE-AFE transition is ferroelectrically switchable. Therefore, this transition is accompanied by a switchable indirect-direct band-gap transition in the $CuInP_2Se_6$ monolayer, which makes the overlayer promising for optical and optoelectronic devices.

In conclusion, we have demonstrated that interface can be an effective way of engineering ferroelectricity in 2D ABP_2X_6 monolayers. In our model, the polarizations of the monolayers are coupled to local dipoles of the substrates and the induced electronic polarizations in the substrate. These couplings can stabilize the FE ordering, that is, they lower (increase) the total energy of one (the other) FE phase while keeping that of the AFE phase almost unchanged. We have applied the strategy to $CuInP_2Se_6$ and $CuCrP_2S_6$ monolayers, for which the energy difference (ΔE) between the FE and the AFE phases are about 12 and 68 meV, respectively. The interfacial interaction between a $CuInP_2Se_6$ monolayer and vdW monolayers, such as MoS_2, graphene, and h-BN, leads to an energy change of 25 ~30 meV for the FE phase and thus can overcome ΔE while keeping the other FE phase as a local minimum of the energy surface. Therefore, a FE switching is feasible for this system, which is supported by our NEB calculations. The vdW interfaces can also drive an AFE-to-FE phase transition for the multilayers of $CuInP_2Se_6$. However, in the case of a $CuCrP_2S_6$ monolayer, a vdW-type interface interaction is found to be insufficient to drive the FE-to-AFE phase transition. Interfacing it to a polar surface MgO(111)

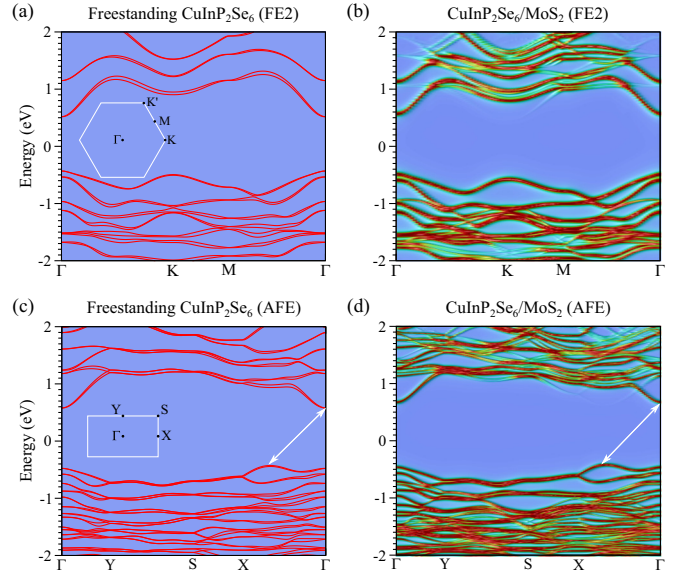can make one of the FE orderings to be energetically lower than the AFE phase, for which a FE switching of different orderings is still likely. We further find a FE switching of electronic structures for $CuInP_2Se_6$- and $CuCrP_2S_6$-based interfaces. Our strategy is universal and can also be applied to other ABP_2X_6 monolayers and 2D materials with out-of-plane charge polarizations. Besides, our study can help to understand the effects of interfacing in devices made of $CuInP_2S_6$ thin films and MoS_2 substrate as already obtained by recent experiments [44,45].

TABLE II. The lattice constants (Å) of different phases for ABP_2X_6 monolayers. For $AgInP_2S_6$ and $AgInP_2Se_6$ monolayers, the structures of the AFE and FE phases were relaxed to that of the PE phase during our DFT calculations.

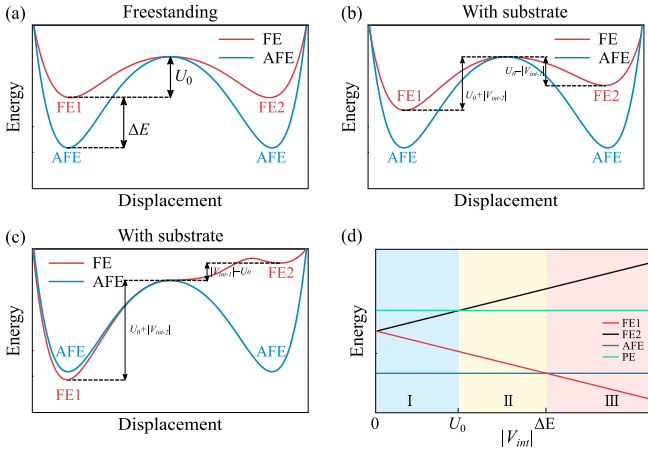| Systems	FE	AFE	PE	Ground state
$CuInP_2S_6$	6.10	6.10	6.05	AFE
$CuInP_2Se_6$	6.42	6.42	6.35	AFE
$CuBiP_2S_6$	6.25	6.28	6.23	FE
$CuBiP_2Se_6$	6.55	6.58	6.55	FE
$CuCrP_2S_6$	6.02	6.02	6.00	AFE
$CuCrP_2Se_6$	6.30	6.28	6.28	AFE
$CuVP_2S_6$	5.98	5.98	5.93	AFE
$CuVP_2Se_6$	6.30	6.30	6.28	AFE
$AgInP_2S_6$	N/A	N/A	6.18	PE
$AgInP_2Se_6$	N/A	N/A	6.48	PE
$AgBiP_2S_6$	6.38	6.38	6.38	FE
$AgBiP_2Se_6$	6.65	6.65	6.63	FE

FIG. 9. The phase diagram of type-II systems under external dipole interactions. (a) Schematic illustration of double-well potentials of a free-standing monolayer for the FE and AFE phases. (b) Energy change of a ABP_2X_6 monolayer with a weak coupling between P and P_{ext} such that $|V_{int}| < \Delta E$. (c) Energy change of a ABP_2X_6 monolayer in the case of $|V_{int}| > \Delta E$. (d) The phase diagram of type-II systems as a function of $|V_{int}|$.

APPENDIX A: LATTICE CONSTANTS OF DIFFERENT PHASES FOR ABP_2X_6

In Table II, we show the optimized lattice constants of different phases for ABP_2X_6 monolayers. One can see that there
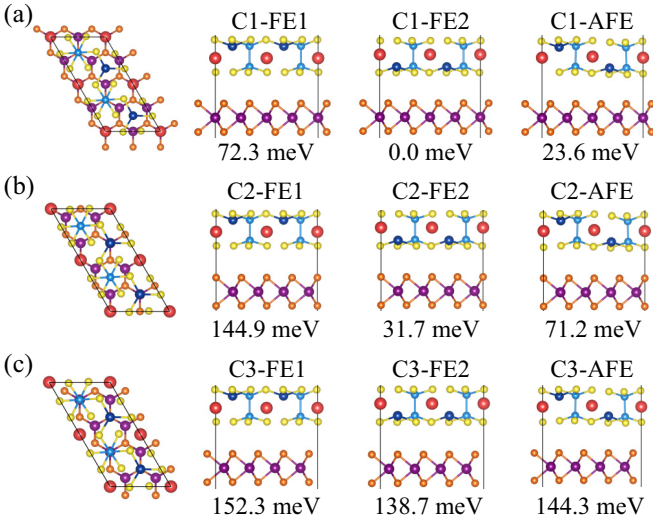

FIG. 10. Top and side views of the structures of $CuInP_2Se_6/MoS_2$ with different polarization states and stackings. Here we only show three high-symmetry stackings named as C1, C2, and C3, respectively. The energy of each structure is given below the structure, for which that of configuration C1-FE2 is taken as the reference.

are little differences in the lattice constant between different phases. Except for $CuInP_2S_6$, the ground states of the ABP_2X_6 monolayers from these calculations are consistent with those shown in Table I obtained from calculations using the lattice constant of the FE phase for AFE and PE phases.

APPENDIX B: THE PHASE DIAGRAM OF TYPE-II SYSTEMS

Figure 9 schematically shows the phase diagram of type-II systems ($\Delta E \geqslant U_0$) under interactions between the ABP_2X_6 monolayers and substrates. The energy potentials of such a system shown in Fig. 9(a) for FE and AFE phases are similar to those for type-I systems [Fig. 2(a)]. The system remains AFE as long as $|V_{int}| < \Delta E$ [Fig. 9(b)]. Strong interactions that give $|V_{int}| > \Delta E$ can turn the system into FE. However, the other FE phase may have an energy higher than the AFE and PE phases [Fig. 9(c)]. The phase diagram shown in Fig. 9(d) is different from that of type-I systems in that the locations of ΔE and U_0 are interchanged.

APPENDIX C: GEOMETRIC STRUCTURES AND ENERGETICS FOR $ABP_2X_6/SUBSTRATES$

Figures 10–12 show the geometric structures of $CuInP_2Se_6/MoS_2$, $CuCrP_2S_6/MoTe_2$, and $CuCrP_2S_6/MgO$, respectively. The energy of each structure relative to that of the ground state structure is also given.
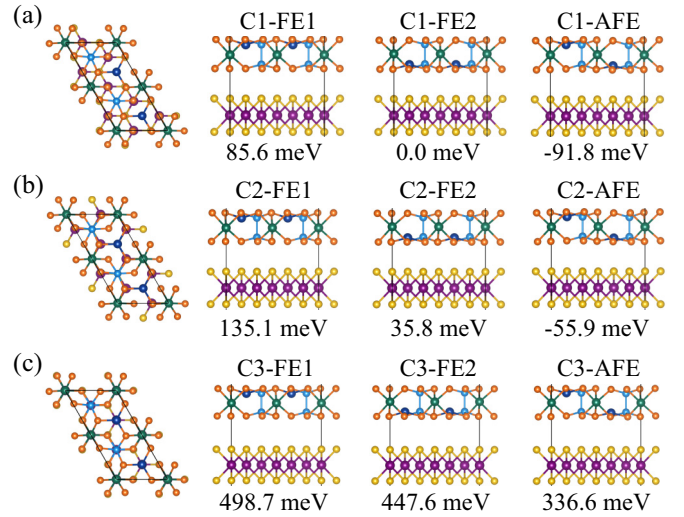

FIG. 11. Geometric structures of $CuCrP_2S_6/MoTe_2$ with different polarization states and stackings. The energy of each configuration relative to that of the ground state C1-FE2 is shown.
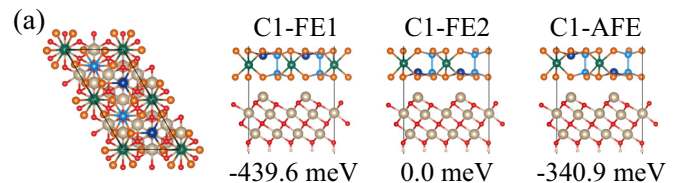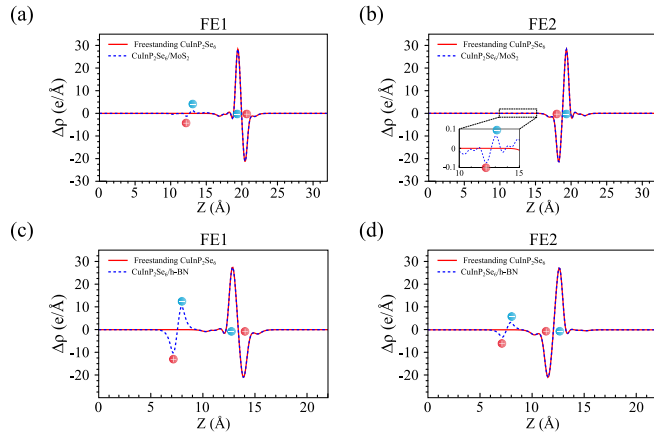

FIG. 12. Geometric structures of $CuCrP_2S_6/MgO(111)$.

FIG. 13. Planar-averaged charge-density difference ($\Delta\rho(z)$) for $CuInP_2Se_6/MoS_2$ and $CuInP_2Se_6/h$-BN in different orderings. The red and blue spheres represent the centers of positive and negative charge densities, respectively.

APPENDIX D: PLANAR-AVERAGED DIFFERENTIAL CHARGE DENSITY

Figure 13 shows the planar-averaged charge-density difference for $CuInP_2Se_6/MoS_2$ and $CuInP_2Se_6/h$-BN. One can see that the induced electronic polarization P_e in MoS_2 is small for both FE orderings. By contrast, P_e in h-BN is comparable to that for $CuInP_2Se_6/$graphene (see Fig. 4).

APPENDIX E: KINETIC PATHWAY OF THE FE PHASE TRANSFORM FOR $CuCrP_2S_6/MgO(111)$

Figure 14 shows the kinetic pathway of FE phase transform for $CuCrP_2S_6/MgO(111)$, which indicates that a FE switching of different orderings is feasible.

APPENDIX F: CALCULATE WITH DIFFERENT VDWS FUNCTIONALS

The results shown in the main text were performed using DFT-D2 functional. In addition, we have carried out calculations using different vdWs functionals/methods for which the results are shown in Table III. One can see that the results
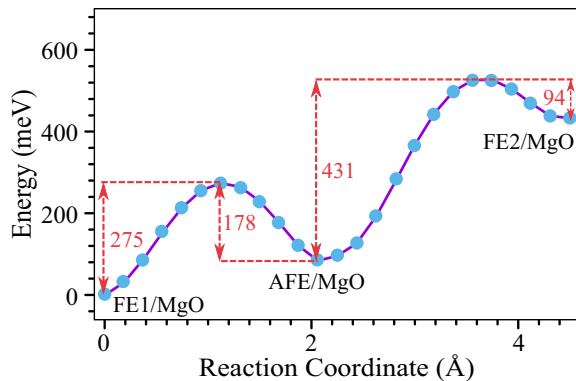

FIG. 14. Kinetic pathway of the FE phase transform in $CuCrP_2S_6/MgO(111)$. Energy barriers are shown in meV.

TABLE III. Energies of different orderings of ABP_2X_6 monolayers and their interfaces with different vdWs functionals/methods. The energies are calculated by taking that of the AFE phase as the reference.

Systems	vdW types	FE1	FE2	AFE	PE
$CuInP_2Se_6$	*	12	12	0	95
$CuInP_2Se_6/MoS_2$	DFT-D2	24	−12	0	101
	DFT-D3	29	−63	0	60
	optPBE	14	−23	0	115
$CuCrP_2S_6$	*	68	68	0	142
$CuCrP_2S_6/MoTe_2$	DFT-D2	92	46	0	151
	DFT-D3	117	39	0	166
	optPBE	92	60	0	127

from different vdWs methods/functionals show essentially the same trend in the stability of different phases.

APPENDIX G: BAND ALIGNMENTS OF $CuInP_2Se_6$ AND $CuCrP_2S_6$ WITH THE SUBSTRATE

We investigate the work functions of the studied systems and their band alignments, for which the results are shown in Fig. 15. One can see that $CuInP_2Se_6$ and MoS_2 as well as h-BN monolayers have a type-I or type-II band alignment for all the orderings. In addition, the Dirac point is located in the band gap of the FE2 and AFE phases of the $CuInP_2Se_6$ when their bands are aligned. So, charge transfers in $CuInP_2Se_6/MoS_2$, $CuInP_2Se_6/$graphene, and $CuInP_2Se_6/h$-BN heterostructures are expected to be negligibly small.
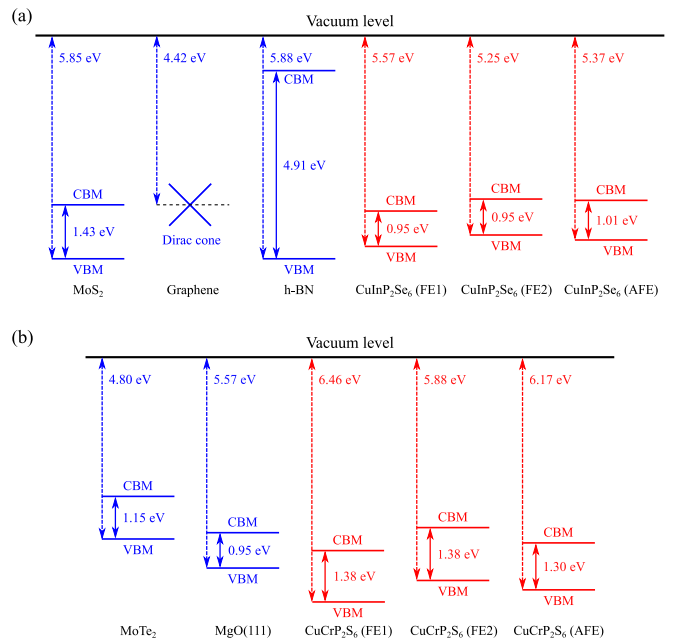

FIG. 15. Band alignments of $CuInP_2Se_6$ and $CuCrP_2S_6$ with the substrate. VBM and CBM denote the valence band maximum and the conduction band minimum, respectively. Work functions and the sizes of the band gaps are given.
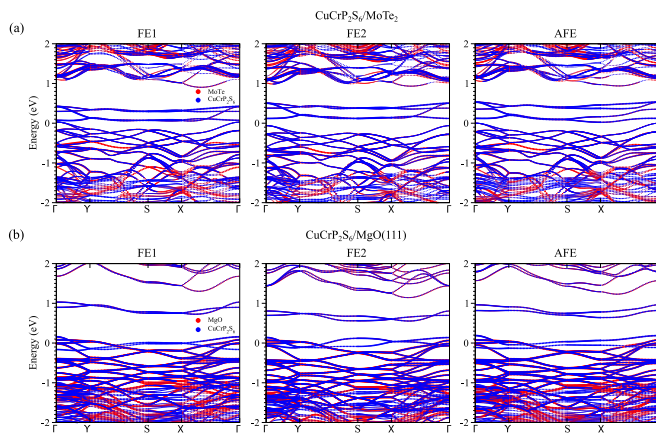
FIG. 16. Effects of a $MoTe_2$ and MgO(111) substrate on the band structure of a $CuCrP_2S_6$ monolayer.

By contrast, $MoTe_2$ has a type-III band alignment with the FE1 phase of the $CuCrP_2S_6$ monolayer and has a type-II band alignment with the FE2 and AFE phases. This behavior helps to understand the band structures shown in Fig. 16. MgO(111) and the $CuCrP_2S_6$ monolayer has a type-II band alignment for all orderings. However, their heterostructures have a metallic band structure, which is due to the strong interfacial bonding.

APPENDIX H: BAND STRUCTURES FOR $CuCrP_2S_6$/$MoTe_2$ AND $CuCrP_2S_6$/MgO(111)

Figure 16 shows the band structures for $CuCrP_2S_6$/$MoTe_2$ and $CuCrP_2S_6$/MgO(111). $CuCrP_2S_6$/$MoTe_2$ remains semiconducting for the AFE and FE2 phases but becomes metallic for the FE1 phase. These behavior can be understood with the help of the band alignments shown in Fig. 15. For $CuCrP_2S_6$/MgO(111), all the band structures for the three orderings indicate that the heterostructure is metallic, which is due to the strong interfacing bonding between the overlayer and the substrate (the interlayer distance is about 2.3 Å).

[1] J. Junquera and P. Ghosez, Nature (London) **422**, 506 (2003).

[2] W. Zhong, R. D. King-Smith, and D. Vanderbilt, Phys. Rev. Lett. **72**, 3618 (1994).

[3] D. D. Fong, G. B. Stephenson, S. K. Streiffer, J. A. Eastman, O. Auciello, P. H. Fuoss, and C. Thompson, Science **304**, 1650 (2004).

[4] M. Stengel, N. A. Spaldin, and D. Vanderbilt, Nat. Phys. **5**, 304 (2010).

[5] E. Almahmoud, I. Kornev, and L. Bellaiche, Phys. Rev. B **81**, 064105 (2010).

[6] K. Chang, J. Liu, H. Lin, N. Wang, K. Zhao, A. Zhang, F. Jin, Y. Zhong, X. Hu, W. Duan, Q. Zhang, L. Fu, Q.-K. Xue, X. Chen, and S.-H. Ji, Science **353**, 274 (2016).

[7] R. Fei, W. Kang, and L. Yang, Phys. Rev. Lett. **117**, 097601 (2016).

[8] N. Higashitarumizu, H. Kawamoto, C.-J. Lee, B.-H. Lin, F.-H. Chu, I. Yonemori, T. Nishimura, K. Wakabayashi, W.-H. Chang, and K. Nagashio, Nat. Commun. **11**, 2428 (2020).

[9] W. Ding, J. Zhu, Z. Wang, Y. Gao, D. Xiao, Y. Gu, Z. Zhang, and W. Zhu, Nat. Commun. **8**, 14956 (2017).

[10] Y. Zhou, D. Wu, Y. Zhu, Y. Cho, Q. He, X. Yang, K. Herrera, Z. Chu, Y. Han, M. C. Downer, H. Peng, and K. Lai, Nano Lett. **17**, 5508 (2017).

[11] C. Cui, W.-J. Hu, X. Yan, C. Addiego, W. Gao, Y. Wang, Z. Wang, L. Li, Y. Cheng, P. Li, X. Zhang, H. N. Alshareef, T. Wu, W. Zhu, X. Pan, and L.-J. Li, Nano Lett. **18**, 1253 (2018).

[12] F. Liu, L. You, K. L. Seyler, X. Li, P. Yu, J. Lin, X. Wang, J. Zhou, H. Wang, H. He, S. T. Pantelides, W. Zhou, P. Sharma, X. Xu, P. M. Ajayan, J. Wang, and Z. Liu, Nat. Commun. **7**, 12357 (2016).

[13] A. Belianinov, Q. He, A. Dziaugys, P. Maksymovych, E. Eliseev, A. Borisevich, A. Morozovska, J. Banys, Y. Vysochanskii, and S. V. Kalinin, Nano Lett. **15**, 3808 (2015).

[14] W. Wan, C. Liu, W. Xiao, and Y. Yao, Appl. Phys. Lett. **111**, 132904 (2017).

[15] B. Xu, H. Xiang, Y. Xia, K. Jiang, X. Wan, J. He, J. Yin, and Z. Liu, Nanoscale **9**, 8427 (2017).

[16] C. Xiao, F. Wang, S. A. Yang, Y. Lu, Y. Feng, and S. Zhang, Adv. Funct. Mater. **28**, 1707383 (2018).

[17] L.-F. Lin, Y. Zhang, A. Moreo, E. Dagotto, and S. Dong, Phys. Rev. Lett. **123**, 067601 (2019).

[18] T. Zhong, X. Li, M. Wu, and J.-M. Liu, Natl. Sci. Rev. **7**, 373 (2019).

[19] C. Xu, P. Chen, H. Tan, Y. Yang, H. Xiang, and L. Bellaiche, Phys. Rev. Lett. **125**, 037203 (2020).

[20] M. Xu, C. Huang, Y. Li, S. Liu, X. Zhong, P. Jena, E. Kan, and Y. Wang, Phys. Rev. Lett. **124**, 067602 (2020).

[21] X.-Y. Ma, H.-Y. Lyu, K.-R. Hao, Y.-M. Zhao, X. Qian, Q.-B. Yan, and G. Su, Sci. Bull. **66**, 233 (2021).

[22] C. Hua, H. Bai, Y. Zheng, Z.-A. Xu, S. A. Yang, Y. Lu, and S.-H. Wei, Chin. Phys. Lett. **38**, 077501 (2021).

[23] H. Bai, X. Wang, W. Wu, P. He, Z. Xu, S. A. Yang, and Y. Lu, Phys. Rev. B **102**, 235403 (2020).

[24] J. Qi, H. Wang, X. Chen, and X. Qian, Appl. Phys. Lett. **113**, 043102 (2018).

[25] Y. Lai, Z. Song, Y. Wan, M. Xue, C. Wang, Y. Ye, L. Dai, Z. Zhang, W. Yang, H. Du, and J. Yang, Nanoscale **11**, 5163 (2019).

[26] W. Song, R. Fei, and L. Yang, Phys. Rev. B **96**, 235420 (2017).

[27] Z.-Z. Sun, W. Xun, L. Jiang, J.-L. Zhong, and Y.-Z. Wu, J. Phys. D: Appl. Phys. **52**, 465302 (2019).

[28] X. Feng, J. Liu, X. Ma, and M. Zhao, Phys. Chem. Chem. Phys. **22**, 7489 (2020).

[29] S. Huang, Z. Shuai, and D. Wang, J. Mater. Chem. A **9**, 2734 (2021).

[30] A. Dziaugys, K. Kelley, J. A. Brehm, L. Tao, A. Puretzky, T. Feng, A. OâHara, S. Neumayer, M. Chyasnavichyus, E. A. Eliseev, J. Banys, Y. Vysochanskii, F. Ye, B. C. Chakoumakos, M. A. Susner, M. A. McGuire, S. V. Kalinin, P. Ganesh, N. Balke, S. T. Pantelides *et al.*, Nat. Commun. **11**, 3623 (2020).

[31] G. Kresse and J. Furthmüller, Phys. Rev. B **54**, 11169 (1996).

[32] P. E. Blöchl, Phys. Rev. B **50**, 17953 (1994).

[33] G. Kresse and D. Joubert, Phys. Rev. B **59**, 1758 (1999).

[34] T. Bucko, J. Hafner, S. Lebegue, and J. G. Angyán, J. Phys. Chem. A **114**, 11814 (2010).

[35] J. Klimeš, D. R. Bowler, and A. Michaelides, J. Phys.: Condens. Matter **22**, 022201 (2009).

[36] J. c. v. Klimeš, D. R. Bowler, and A. Michaelides, Phys. Rev. B **83**, 195131 (2011).

[37] M. X. Chen and M. Weinert, Nano Lett. **14**, 5189 (2014).

[38] M. X. Chen, W. Chen, Z. Zhang, and M. Weinert, Phys. Rev. B **96**, 245111 (2017).

[39] M. Chen and M. Weinert, Phys. Rev. B **98**, 245421 (2018).

[40] G. Henkelman, B. P. Uberuaga, and H. Jónsson, J. Chem. Phys. **113**, 9901 (2000).

[41] S. L. Dudarev, G. A. Botton, S. Y. Savrasov, C. J. Humphreys, and A. P. Sutton, Phys. Rev. B **57**, 1505 (1998).

[42] F. Finocchi, A. Barbier, J. Jupille, and C. Noguera, Phys. Rev. Lett. **92**, 136101 (2004).

[43] W.-B. Zhang and B.-Y. Tang, J. Phys. Chem. C **112**, 3327 (2008).

[44] M. Si, P.-Y. Liao, G. Qiu, Y. Duan, and P. D. Ye, ACS Nano **12**, 6700 (2018).

[45] X. Wang, C. Zhu, Y. Deng, R. Duan, J. Chen, Q. Zeng, J. Zhou, Q. Fu, L. You, S. Liu, J. H. Edgar, P. Yu, and Z. Liu, Nat. Commun. **12**, 1109 (2021).